applied sciences

MDPI

Article

A Cylinder-Type Multimodal Traveling Wave Piezoelectric Actuator

Dalius Mažeika [1], Andrius Čeponis [2,*] and Daiva Makutėnienė [2]

[1] Department of Information Systems, Faculty of Fundamental Sciences, Vilnius Gediminas Technical University, Sauletekio avn. 11, LT-10223 Vilnius, Lithuania; dalius.mazeika@vgtu.lt

[2] Department of Engineering Graphics, Faculty of Fundamental Sciences, Vilnius Gediminas Technical University, Sauletekio avn. 11, LT-10223 Vilnius, Lithuania; daiva.makuteniene@vgtu.lt

* Correspondence: andrius.ceponis@vgtu.lt; Tel.: +370-6-221-4611

Received: 27 February 2020; Accepted: 30 March 2020; Published: 1 April 2020

Abstract: Numerical and experimental investigations of a multimodal piezoelectric traveling wave actuator are presented. The actuator consists of a cylindrical stator with a conical hole and piezoceramic rings that are located at the node of the first longitudinal and second bending vibration modes; one piezoceramic ring is also placed at the bottom of the actuator. The actuator is clamped at the bottom using a special supporting cylinder and a ball bearing. Traveling-wave-type vibrations are excited at the top surface of the cylinder by employing a superposition of the first longitudinal and second bending vibration modes of the stator. The conical hole of the stator is used to amplify the vibration amplitudes of the contact surface. Four electric signals with phase difference of $\pi/2$ are used to drive the actuator. Numerical and experimental investigations showed that the proposed actuator is able to generate up to 115 RPM rotation speed at constant preload force.

Keywords: piezoelectric actuator; traveling wave; hybrid vibrations; mode superposition

1. Introduction

Traveling wave actuators are one of the most popular piezoelectric devices that are used in numerous industrial, medical, and life-science fields [1,2]. This type of actuator has features like high accuracy, microscale resolution, self-locking, high torque, and quick response [3–5]. Usually, the operating principle of traveling wave actuators is based on the excitation of traveling wave vibrations in a ring-type stator [6–8]. However, the amplitudes of the contact surface vibrations of such stators are low. Therefore, toothed ring-shaped stators are used. The configuration of the tooth, including height, cross section, and shape, is based on the mechanical output requirements of the motor. However, the tooth-based stators have height limitations because of buckling phenomena [9–11]. Buckling occurs when the preload force between the stator and rotor increases and exceeds the critical load. In this case, uncontrolled slipping between the stator and rotor appears, energy losses and wear at the contact area increase, and, as a result, the performance and reliability of the actuator decreases [12]. Moreover, these disadvantages limit the design flexibility of the stator and, as a result, possible application areas of the traveling wave actuators. Therefore, to overcome these disadvantages of toothed stators, toothless traveling wave actuators should be introduced.

Kanda et al. reported a cylindrical traveling wave actuator based on a micromachined bulk vibrator and glass case [13]. The operating principle of this actuator is based on the first or second out-of-plane bending vibration modes of the step-shaped cylinder. The excitation of the actuator is performed using four signals which have a phase difference of $\pi/2$. On the basis of numerical and experimental investigations, the authors concluded that the proposed motor can achieve a rotational velocity of 1000 RPM with excitation signal frequency and amplitude of 67 kHz and 40 $V_{p\text{-}p}$, respectively.

The authors also performed numerical investigations of when the motor was driven at higher vibration mode and concluded that usage of a higher vibration mode could increase the performance of the motor.

Dong et al. reported a rotary traveling wave actuator with design based on a toothless stator and rotor pair with irregular cross sections [14]. The cross sections of the stator and rotor were modified by cylindrical cavities. The modifications were made in order to increase the displacement amplitudes of the actuator and overcome buckling phenomena. This actuator's operation is based on synchronous traveling wave vibrations in the modified stator and rotor. The authors concluded that the proposed approach could increase the mechanical performance and design flexibility of simple traveling wave actuators, as well as overcome the disadvantages of tooth-based traveling wave actuators.

Jin and Zhao reported a toothless traveling wave rotary motor based on a ring-shaped stator, bar-shaped transducer, and two-sided rotors [15]. The simple design of the stator and separated heat source and friction interface make the motor more attractive compared to the conventional design of traveling wave motors. Employment of the proposed toothless stator eliminates the disadvantages related to tooth buckling phenomena and makes the design more flexible and easily customizable to special requirements. The authors performed numerical and experimental investigations of the motor and concluded that the proposed motor can operate in both longitudinal and bending vibration modes. According to the results, the motor is able to provide 0.25 Nm and 50 r/min at a frequency of 48.625 kHz when an excitation voltage of 300 $V_{p\text{-}p}$ is applied.

Ting et al. reported a 2-degree-of-freedom (DOF) piezoelectric toothless traveling wave rotary motor [16]. The motor design is based on a hemispherical stator with two sets of piezoelectric patches. The patches are located on the outside surface of the stator and have a radial distribution of 90°. Moreover, the linear distribution of the patches corresponds to $\lambda/4$ for each group. The motor has a simple design and can be scaled depending on the requirements. The authors investigated eight vibration modes that are potentially suitable for high-performance operation of the motor and concluded that the best performance was achieved at a frequency of 44 kHz, corresponding to the sixth vibration mode of the stator. A resolution of 23 μm and an angular velocity of 25°/s were achieved when the motor was driven at this frequency.

This work presents our further investigation into a traveling wave actuator with operation based on the superposition of the first longitudinal and second bending vibration modes of the waveguide [17]. The actuator was redesigned and improved to obtain more efficient excitation of the first longitudinal vibration mode and to improve the mechanical and electrical characteristics of the actuator. For this purpose, two additional piezoceramic rings were placed at the node of the two vibration modes. The optimization problem was solved to obtain optimal dimensions when the difference between the resonant frequencies of the second bending and the first longitudinal modes was minimized. Two geometrical parameters of the stator were included in the optimization problem: the upper diameter of the conical cavity (D_{in}) and the height of the waveguide (H). Also, numerical and experimental investigations of the proposed piezoelectric actuator were performed in order to validate the operating principle, as well as to analyze the mechanical and electrical characteristics of the actuator.

2. Design and Operation Principle of the Actuator

The actuator presented herein consists of a cylindrical waveguide with a conical hole inside, three piezoceramic rings, and a clamping system (Figure 1). The waveguide is composed of two parts that are joined by a thread junction. Such a waveguide configuration is used to locate a piezoceramic ring at a node of longitudinal vibrations of the waveguide. The waveguide was made from aluminum alloy 6061, and PZT8 hard piezoceramic rings were used for the actuation. The two piezoceramic rings were located at the node of the first longitudinal and second bending vibration modes, while one ring was glued at the bottom of the waveguide. The clamping system was located at the bottom of the waveguide and consists of a supporting cylinder, a ball bearing, a ball bearing bed, a fixing

bolt, and a fixing ring. A schematic of the actuator is shown in Figure 1. The main dimensions of the actuator are given in Table 1.

Table 1. Dimensions of the actuator.

Parameter	Value	Description
D_{in}	17 mm	Upper diameter of the conical hole
D	20 mm	Outer diameter of the waveguide
α	9.86°	Inclination of the conical hole
H	49 mm	Height of the waveguide
H_c	41 mm	Height of the conical cavity
H_{pzt}	3 mm	Thickness of the piezoceramic rings
H_n	21 mm	Distance to the node center of the vibration modes
H_{total}	67.5 mm	Total height of the actuator

The dimensions of the actuator were obtained by numerical modeling and are described in detail in the next section. The conical hole of the waveguide was designed to amplify displacement and velocity amplitudes at the top surface of the waveguide. Moreover, due to the nonuniform stiffness of the waveguide, the node of the first longitudinal and second bending vibration modes was shifted down from the center of the cylinder; as a result, displacement amplitudes are amplified additionally because of the increased lever arm.

The clamping system of the actuator operates as a counter-loosening system for the clamping bolt and composes the supporting cylinder that is placed at the center of the waveguide bottom. The supporting cylinder is clamped to the waveguide using an M3 bolt, while the other end of the supporting cylinder is put to the inner face of the ball bearing. The outer ring of the ball bearing is clamped into the ball bearing bed rigidly. Such a clamping system prevents possible loosening of the clamping force applied to the M3 bolt during actuator operation.

The operating principle of the actuator is based on the superposition of the second bending and the first longitudinal vibration modes. Excitation of the second bending vibration mode is performed by the piezoceramic ring which was glued at the bottom of the waveguide, while the first longitudinal vibration mode is excited by two piezoceramic rings which were placed at the node of the first longitudinal mode. (Figure 1a). Excitation of the second bending vibration mode by piezoceramic placed at the bottom of the waveguide ensures generation of the traveling wave. For this purpose, the electrode of the piezoceramic ring was divided in four equal sections which are effected by four harmonic signals with phase difference $\pi/2$ (Figure 1b). Such an arrangement of the excitation signals ensures that the waveguide sequentially bends in accordance with the phase of the excitation signals; in this way, an even traveling wave is generated in the clockwise direction on the top surface of the waveguide. In order to generate a traveling wave in the counterclockwise direction, the phases of the excitation signals must be changed by π. Moreover, the conical hole which was made in the waveguide amplifies vibrations of the traveling wave due to the nonuniform stiffness of the waveguide, i.e., the stiffness at the top of the waveguide is lower compared to that at the bottom of the waveguide. To amplify displacements in the axial direction, the first longitudinal vibration mode of the waveguide is excited by two piezoceramic rings which were located at the node of the vibration mode. The first longitudinal vibration mode is excited by a single harmonic signal (Figure 1b). Therefore, it can be assumed that the traveling wave generated on the top surface of the waveguide has additional motion in a longitudinal direction, which improves the dynamic characteristics of the actuator.

It can be summarized that the proposed piezoelectric actuator has the following advantages: amplification of the vibration amplitudes at the contact interface because of the conical hole of the waveguide, more effective excitation of the first longitudinal vibrations compared to the actuator proposed in [17], and more precise dimensions that allowed us to achieve better superposition of the first and second vibration modes.

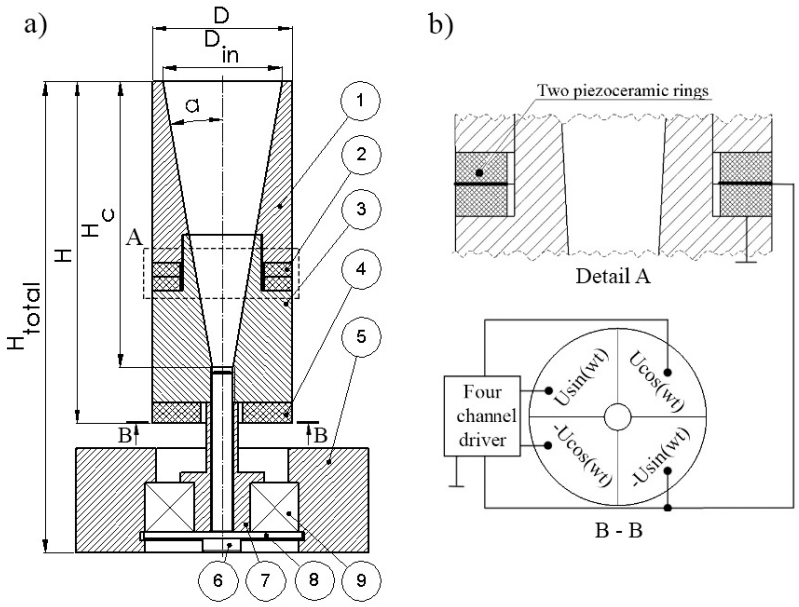

Figure 1. Schematics and excitation scheme of the traveling wave actuator: (**a**) Schematics of the traveling wave actuator: 1, the upper part of the waveguide; 2, the piezoceramic rings placed at the node; 3, the lower part of the waveguide; 4, the piezoceramic ring placed at the bottom of the waveguide; 5, the ball-bearing bed; 6, M3 fixing bolt; 7, the supporting cylinder; 8, the fixing ring; 9, the ball bearing. (**b**) Excitation scheme of the actuator.

3. Numerical Investigation of the Actuator

Numerical investigations were performed to find the optimal dimensions of the actuator, to verify the operation principle, and to investigate the mechanical and electrical characteristics of the actuator. Comsol Multiphysics 5.4 software (v5.4, Comsol AB, Stockholm, Sweden) was used for the modeling. The material properties used for the modeling are presented in Table 2.

Table 2. Properties of the materials.

Material Property	PZT8	6061 Aluminum Alloy
Density [kg/m^3]	7800	2700
Young's modulus [N/m^2]	7.6×10^{10}	7×10^{10}
Poisson's ratio	-	0.33
Isotropic structural loss factor	-	0.001
Relative permittivity	$\varepsilon_{33}{}^{T}/\varepsilon_0 = 1200$ $\varepsilon_{11}{}^{T}/\varepsilon_0 = 1500$	-
Piezoelectric constant d_{33} [10^{-12} m/V]	225	-
Piezoelectric constant d_{31} [10^{-12} m/V]	−97	-
Piezoelectric constant d_{15} [10^{-12} m/V]	330	-
Elastic stiffness coefficient $C_{33}{}^{D}$ [N/m^2]	1.6×10^{10}	-

Firstly, the dimensions of the actuator were optimized in order to minimize the difference between the natural frequencies of the first longitudinal and second bending vibration modes. The optimal dimensions of the actuator allow us to achieve superposition of the vibration modes. The height of the waveguide H and the upper diameter of the conical cavity D_{in} were selected as design variables, while other parameters were set as shown in Table 1. The optimization problem can be written as follows:

$$\min_{\Delta f}(\Delta f = \left|w_{L_1}(H, D_{in}) - w_{B_2}(H, D_{in})\right|); \quad (1)$$

subject to

$$h_{\min} \leq H \leq h_{\max}; \tag{2}$$

$$d_{\min} \leq D_{in} \leq d_{\max}; \tag{3}$$

$$H_c(H) = H - h_{offset} \tag{4}$$

where H is the height of the waveguide; D_{in} is the diameter of the conical hole; Δf is the difference in the natural frequencies of the first longitudinal and second bending vibration modes; w_{L1} is the natural frequency of the first longitudinal vibration mode; w_{B2} is the natural frequency of the second bending vibration mode; h_{min} and h_{max} are the minimum and maximum values of waveguide height; d_{min} and d_{max} are the minimum and maximum values of the base diameter of the conical hole; H_c is the height of the conical cavity; and h_{offset} is 8 mm, and it is the offset of the conical cavity from the bottom surface of the waveguide. The following boundary values of the design variables were used: h_{min} = 35 mm, h_{max} = 57 mm, d_{min} = 12 mm, d_{max} = 18 mm.

Modal frequency analysis of the actuator was performed during optimization. The boundary conditions were as follows: A fixed constraint was added in order to simulate the clamping system of the actuator. The actuator was loaded by gravity force. The linear search algorithm was applied for the calculations, while a step size of 0.5 mm was used for both design variables. The plot shown in Figure 2 presents the results of calculations.

The difference between the natural frequencies varied from 43 Hz to 3850 Hz, and it depended on the combination of values of the design variables (Figure 2). The four best sets of design variable values are listed in Table 3. The difference in the natural frequencies for these sets varied from 43 Hz to 66 Hz. This shows that superposition of the vibration modes can be obtained using several sets of variables. The design variable values of H =49 mm and D_{in} = 16.5 mm were chosen for further investigation because they provided the lowest difference between the natural frequencies. Frequency values of 51202 Hz and 51245 Hz were obtained for the first longitudinal and the second bending vibration modes, respectively. A view of the vibration modes is given in Figure 3.

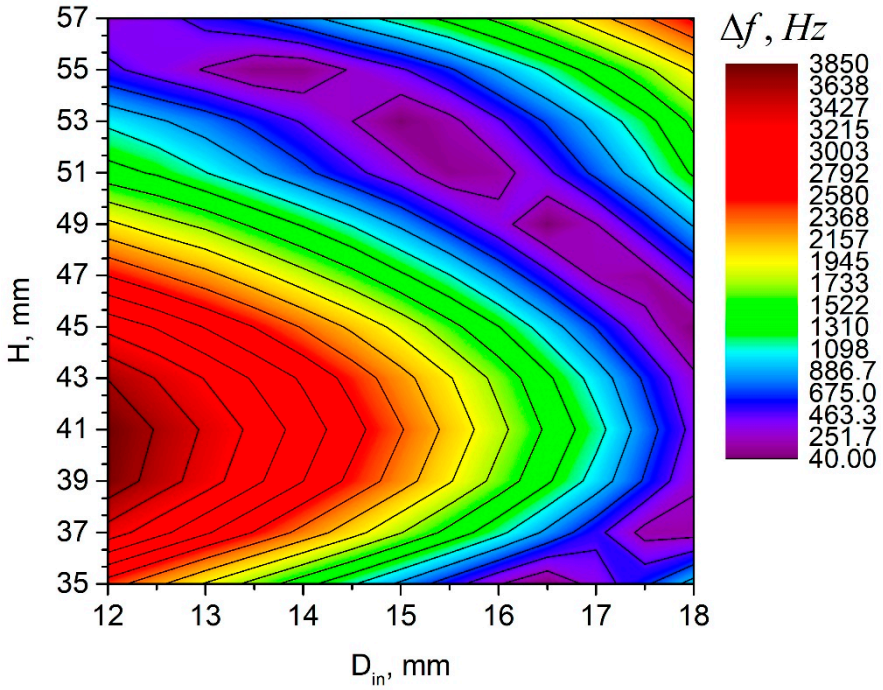

Figure 2. Dependence of the difference between the natural frequencies of the first longitudinal and second bending vibration modes on the diameter of the hole and height of the cylinder.

Table 3. The values of design variables and optimization criteria.

Geometrical Parameters	The First Longitudinal Vibration Mode, Hz	The Second Bending Vibration Mode, Hz	$\Delta f = \lvert w_{L1} - w_{B2} \rvert, Hz$
H = 35 mm; D_{in} = 16.5 mm	66,246	66,190	56
H = 45 mm; D_{in} = 18 mm	55,937	55,878	59
H = 49 mm; D_{in} = 16.5 mm	51,202	51,245	43
H = 53 mm; D_{in} = 15 mm	46,931	46,997	66

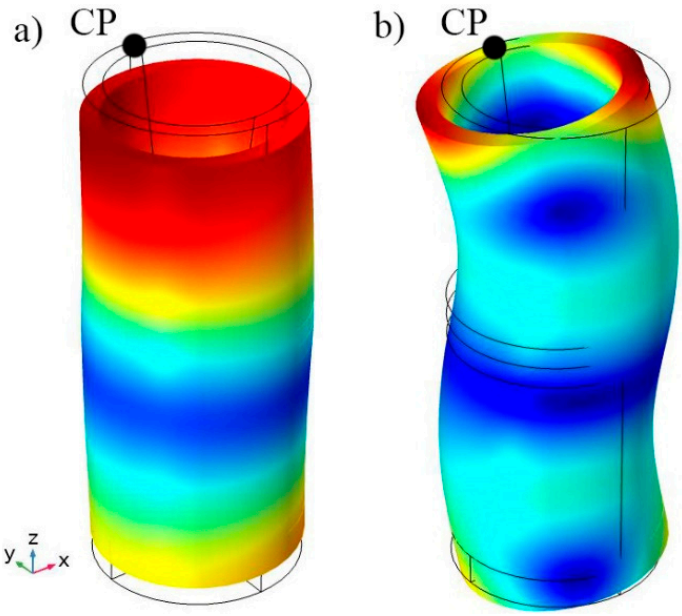

Figure 3. The vibration modes of the waveguide; (**a**) the first longitudinal vibration mode at 51,202 Hz; (**b**) the second bending vibration mode at 51,245 Hz; CP, contact point.

The next step of the numerical study was to investigate the electrical and mechanical characteristics of the actuator. The displacement and velocity amplitudes of the contact point were analyzed. Moreover, the motion trajectories of the contact point (CP) were calculated. Also, analysis of the impedance–frequency and phase–frequency characteristics was performed. In order to obtain these characteristics, the same numerical model of the actuator was analyzed in the frequency and time domains. Firstly, the impedance–frequency and phase–frequency characteristics were calculated to obtain the electrical characteristics of the actuator. The results of the investigation are given in Figure 4.

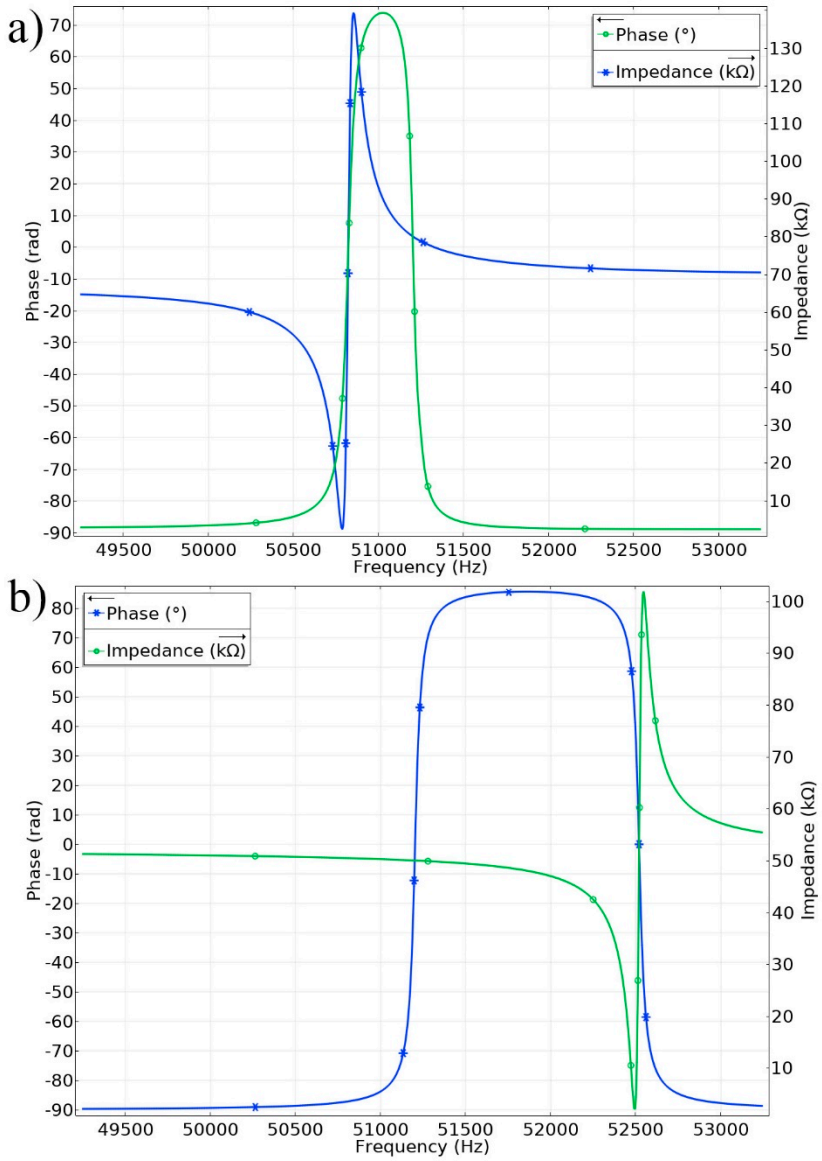

Figure 4. Impedance–frequency and phase–frequency characteristics of the actuator: (**a**) the characteristics of the first longitudinal vibration mode; (**b**) the characteristics of the second bending vibration mode.

By analyzing the results, it can be noted that the impedance values of the actuator at the first longitudinal and second bending vibration modes were 2.35 kΩ and 2.15 kΩ, respectively. Similar impedance values at the resonant frequency show that damping of the actuator is similar when both vibration modes are excited. Also, low values of impedance show that the actuator has high-efficiency electrical energy conversion.

The amplitude–frequency and velocity–frequency characteristics of the contact point were studied as well. The amplitude of the excitation voltage was set to 200 $V_{p\text{-}p}$ while excitation signals were applied to the piezoceramic rings, as shown in Figure 1b. The frequency range from 49 kHz to 54 kHz with a frequency step of 5 Hz was analyzed. The displacement and velocity amplitudes of the contact point located on the top surface of the waveguide were analyzed. The graph related to the displacement amplitudes is given in Figure 5. An analysis of the velocity amplitudes is given below Figure 5.

The graphs in Figure 5 show that the actuator generates displacements in the X, Y, and Z directions. Also, it can be pointed out that the first longitudinal and second bending modes of the actuator are excited simultaneously. The amplitude peak in the Z direction is slightly shifted down in the frequency

domain compared to the other peaks. The difference between peaks is 42 Hz. The displacement amplitude in the Z direction is 47.53 µm, while those in the X and Y directions are 6.24 µm and 3.1 µm, respectively. The ratio between displacement amplitudes in the X and Y directions is 2.01, while the ratio between displacement amplitudes in the Z and X or Y directions is approximately 7.61. The velocity–frequency characteristics of the contact point motion were calculated as well. It was found that peaks of the velocity amplitudes are at the same frequencies as those in the displacement–frequency characteristics. The velocity amplitudes of the contact point are 15.3 m/s, 0.98 m/s, and 2.01 m/s in the Z, X, and Y directions, respectively. The ratio between velocity amplitudes in the X and Y directions is 2.05, while the ratio between the Z and X or Y directions is approximately 7.61.

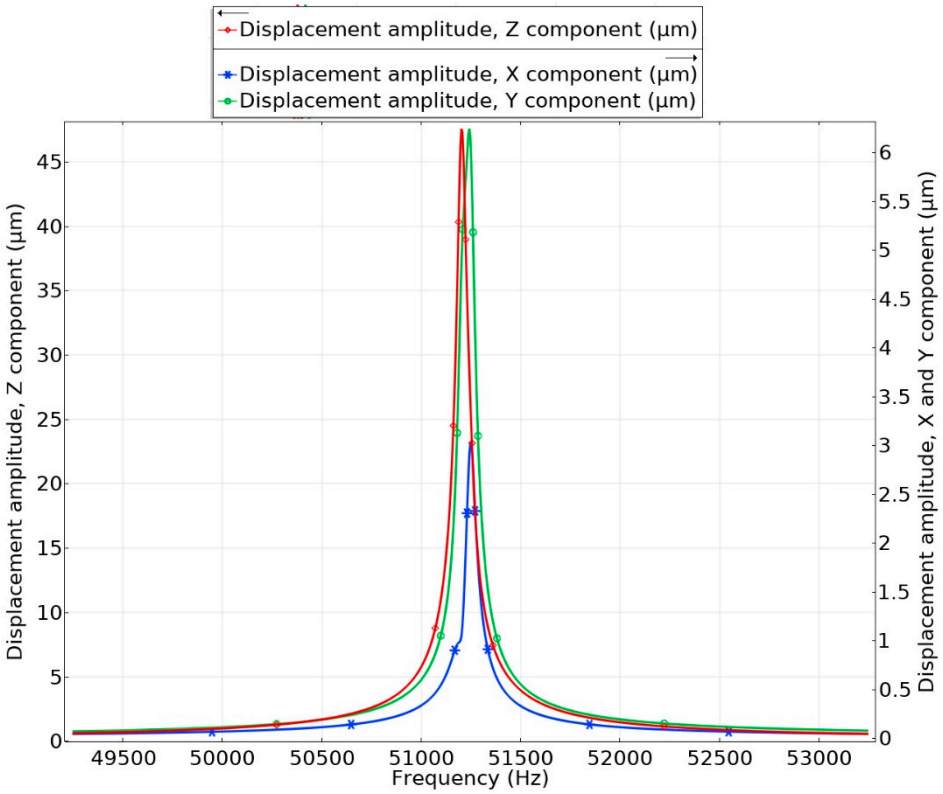

Figure 5. Amplitude–frequency characteristics of the contact point.

The contact point motion trajectories in the XY, YZ, and XZ planes were calculated. A time domain study was used for this purpose. A time range equal to one period of the resonance frequency was analyzed while a time step of 0.25 µs was used. The same excitation scheme of the actuator as that in the frequency domain study was used. The results are shown in Figure 6.

It can be seen that the contact point trajectories are close to an elliptical shape and have different lengths of the major axis and rotation angle to the horizontal axis. The contact point motion trajectory in the XY plane shows that the displacement projection in the Y axis is 1.94 times larger compared to displacement in the X axis. This trajectory mainly represents displacement generated by the second bending vibration mode.

The contact point trajectory in the XZ plane has notably higher displacement compared to that in the XY plane (Figure 6a). The length of trajectory projection in the X axis is 13.2 µm, while that in the Z axis is 92.5 µm. The ratio between displacements is around 7. It can be concluded that the superposition of the first longitudinal and second bending vibration modes ensures higher displacement compared to that generated by a single second bending vibration mode.

The contact point trajectory in the YZ plane has the highest major axis length compared to the trajectory projections of the XY and XZ planes. The length of trajectory projection in the Y axis is 6.45

µm, and the projection in the Z axis is 93.25 µm. The ratio between displacement projections in the Y and Z axes is 14.45. These results show that displacement fields generated only by the second bending mode in the XY plane are notably lower compared to displacement fields generated in the YZ plane during actuator operation in the superposition mode.

Based on the results of the numerical study, it can be concluded that traveling wave displacements generated by the second bending vibration mode are modified by displacements of the first longitudinal vibration mode and can be used to rotate a rotor.

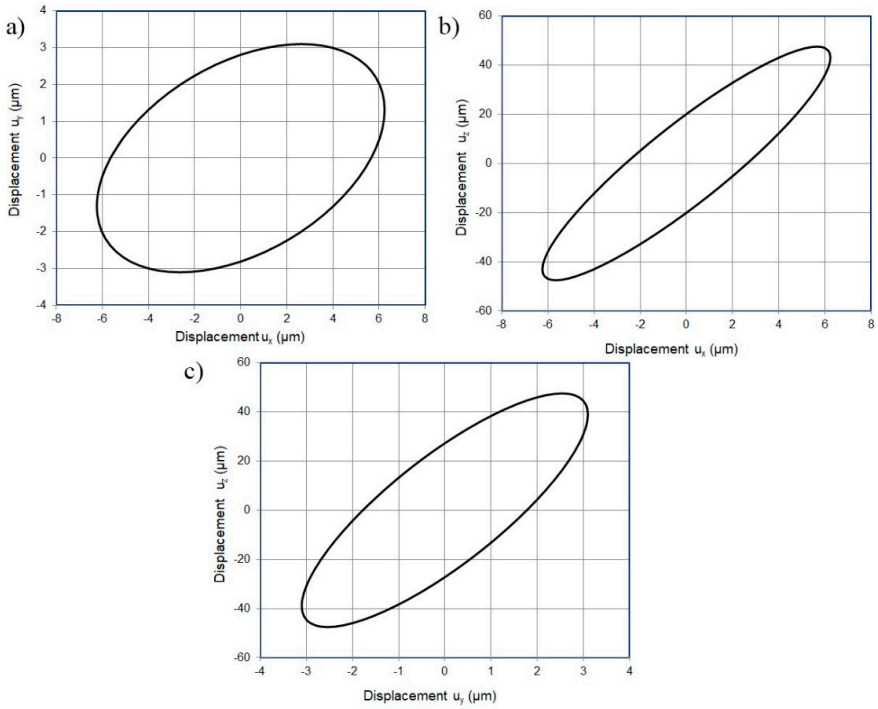

Figure 6. Displacement trajectories of the contact point: (**a**) in the XY plane; (**b**) in the XZ plane; (**c**) in the YZ plane.

4. Experimental Investigation of the Traveling Wave Actuator

A prototype was made in order to perform experimental investigations and verify the operating principle of the actuator (Figure 7). The dimensions and material parameters of the prototype were the same as those shown in Tables 1–3.

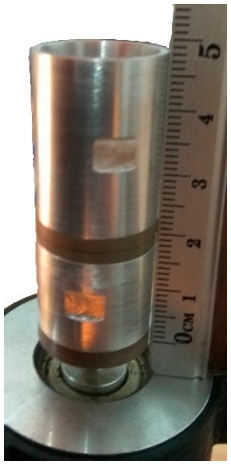

Figure 7. Prototype of the traveling wave actuator.

Firstly, measurements of the impedance–frequency and phase–frequency characteristics were performed. A 4192A impedance analyzer (HP, Palo Alto, CA, USA) was used for this purpose. The results of the measurement are shown in Figure 8. Two resonance frequencies can be seen in the plot. The first longitudinal vibration mode has a frequency of 51.75 kHz, while the second bending vibration mode has a frequency of 52.35 kHz. The difference between the resonance frequencies is 600 Hz. Compared to the results of modal analysis, this difference is notably higher. It is mainly caused by manufacturing errors, as well as slight differences in the material properties and actuator clamping.

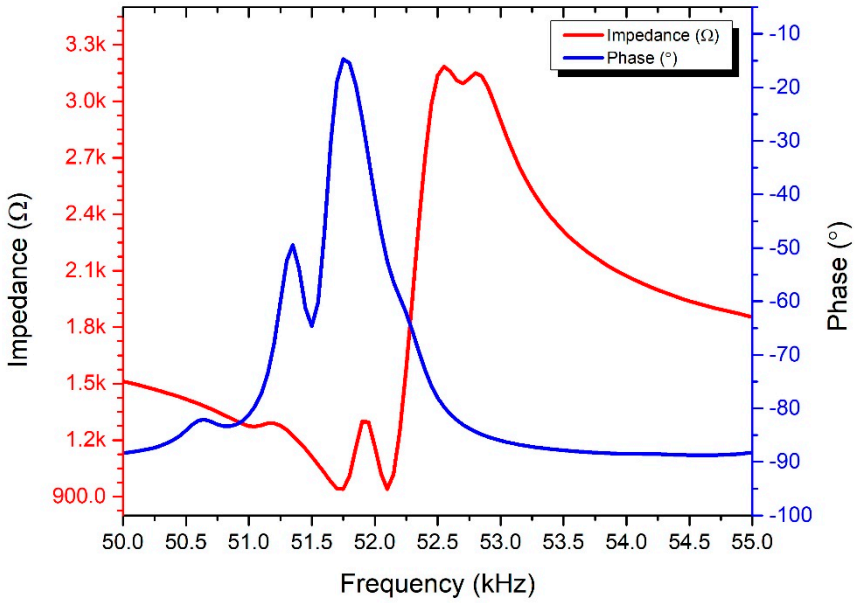

Figure 8. Measured impedance–frequency and phase–frequency characteristics.

Also, it can be noted that the impedance values at the resonance frequencies have a small difference. The impedance at the first longitudinal vibration mode is 1.1 kΩ, while that at the second bending vibration mode is 1.03 kΩ. The difference is 700 Ω. Comparing the impedance values obtained numerically and experimentally, a difference of 1 kΩ was obtained.

The mechanical characteristics of the actuator were measured as well. The experimental study was split into the following steps: experimental verification of the operating principle, measurements of the contact point displacement amplitudes in the XYZ directions, and rotation speed measurements. Firstly, experimental verification of the operating principle was performed. For this purpose, a PSV-500 scanning vibrometer was used (Polytec, Waldbronn, Germany). The goal of the measurements was to obtain trajectories of the contact point (CP) motion. The top surface displacements of the actuator were measured during one period of vibrations. The results of the measurements at 51.65 kHz are given in Figure 9.

Figure 9 presents the motion of the contact point in $2\frac{1}{2}\pi$ and presents a visualization of the vibrations on the top surface of the waveguide. It can be seen that the contact point vibration has a harmonic form. So, in accordance with the excitation scheme (Figure 1b), it can be concluded that a traveling wave is generated on the top surface of the waveguide. Also, the visualization shows that the traveling wave has additional motion in the longitudinal direction. Therefore, it shows that the first longitudinal vibration mode is excited as well.

The contact point velocity and displacement amplitudes in the XYZ directions were measured as well. For this purpose, an experimental setup was built (Figure 10). It included a WW5064 four-channel function generator (Tabor Electronics, Israel), an E-619 power amplifier (PI Ceramic GmbH, Lederhose, Germany), a Yokogawa DL2000 four-channel oscilloscope (Yokogawa, Tokyo, Japan), a UT 372 noncontact tachometer (Uni-T, Dongguan, China), and a U3B proximity sensor (Lion

Precision, Oakdale, MN, USA) that was used to measure velocity and displacement amplitudes of the waveguide in the XYZ directions. Finally, a computer was used to record and manage the data.

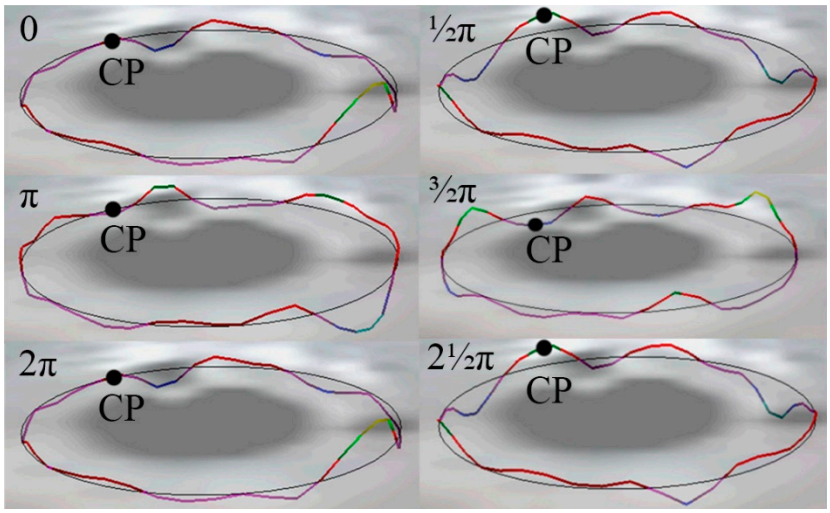

Figure 9. Displacement trajectory of the contact point over time; CP is a contact point.

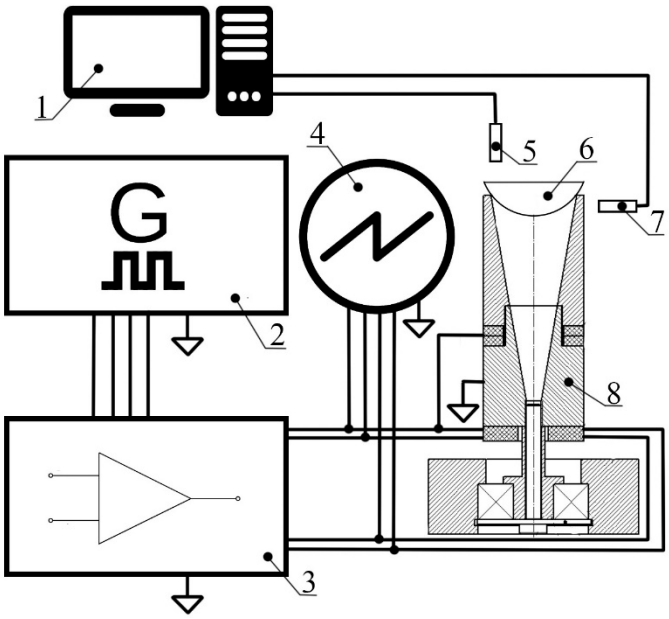

Figure 10. Experimental setup: 1, a computer with data acquisition software; 2, four-channel function generator; 3, four-channel power amplifier; 4, oscilloscope; 5, noncontact tachometer; 6, spherical rotor; 7, proximity sensor; 8, traveling wave actuator.

The results of contact point displacement trajectory measurements in the XYZ directions under different excitation voltages are given in Figure 11. It must be noted that three different points were measured; the measured points were located on the outside surfaces of the actuator for measurement in the X and Y directions, while a point located on the top surface of the actuator was measured in the Z direction. A schematic of the measurements is given in Figure 12.

Analysis of Figure 11a revealed that the contact point has an elliptical displacement trajectory in the XY plane at different amplitudes of excitation voltages. The displacement amplitude in the X direction at 100 V excitation voltage is in the range from −42 μm to 41 μm, while that in the Y direction is from −64 μm to 60 μm. On the other hand, alternations in displacements at other excitation voltages are in the range from 126 μm to 164 μm in the X direction, while those in the Y direction are from 135

µm to 180 µm. It can be noted that the ratio between the increment of excitation voltage and generated displacements is low. The low ratio between excitation voltage increment and displacement amplitudes is influenced by geometrical parameters of the waveguide, i.e., displacement amplitudes generated by the second bending mode are suppressed by high stiffness of the waveguide, which is directly related to the diameter of the waveguide and ratio of the conical hole. On the other hand, the characteristics of displacement amplitudes in the XY directions show that the most effective excitation voltage for the actuator is 250 V because it exhibits the best ratio of displacement amplitude to excitation voltage, 0.656 µm/V.

Figure 11b presents contact point trajectories in the XZ plane. The characteristics represent actuator operation in the superposition mode, i.e., the displacement trajectories are generated by the first longitudinal and second bending vibration modes. As can be seen in the graph, the lowest displacement amplitudes were obtained at an excitation voltage of 100 V. The displacements are in the range from −42 µm to 41 µm in the X direction, while the Z-direction displacement amplitudes are in the range from −83 µm to 84 µm. As in the case before, it can be seen that the impact of excitation voltage on displacement amplitudes is drastically reduced when the excitation voltage becomes higher than 250 V. Therefore, the ratio of displacement amplitude to excitation voltage is the best at 250 V, i.e., 0.668 µm/V.

Figure 11c presents contact point trajectories in the YZ plane. As in the previous case, the characteristics illustrate actuator operation in the superposition mode. The lowest displacement amplitudes were obtained at 100 V and are in the range from −64 µm to 60 µm in the Y direction, while Z-direction displacement amplitudes are in the range from −86 µm to 87 µm. The best ratio of displacement amplitude to excitation voltage was obtained at 250 V as in the previous case, i.e., 0.692 µm/V.

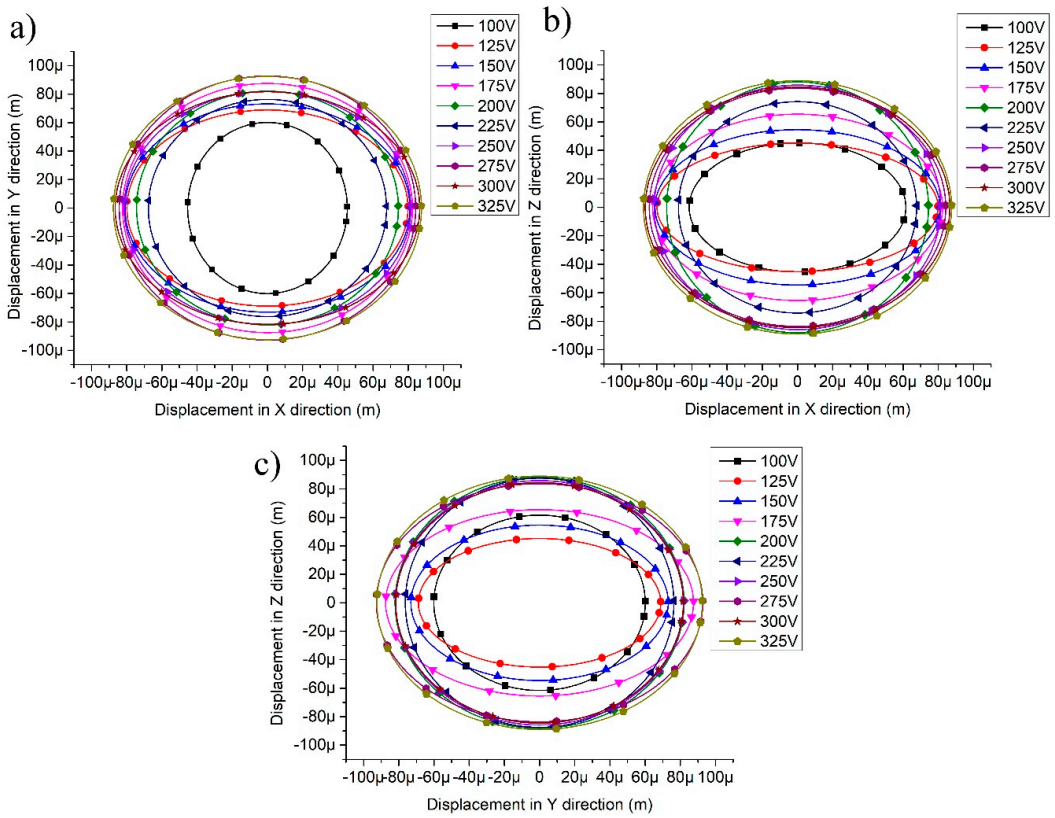

Figure 11. Trajectories of the contact point when different voltages are applied; (**a**) the trajectory of a contact point in the XY plane; (**b**) the trajectory of a contact point in the XZ plane; (**c**) the trajectory of a contact point in the YZ plane.

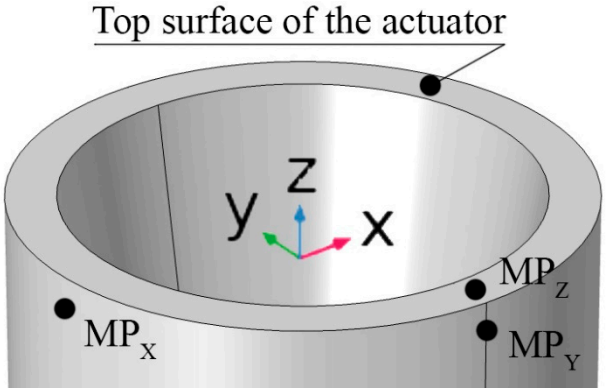

Figure 12. Schematics of displacement amplitude measurements in different planes; MP, measurement point.

The next step of the experimental study was to measure the contact point velocities in the XYZ directions. The same experimental setup, as shown in Figure 10, was used. The measurements of the contact point velocity were made in the range from 25 V to 70 V. Such a range of the excitation voltage was chosen in order to represent contact point response to low excitation voltage. The results are shown in Figure 13.

Analysis of Figure 13 showed that the highest velocity amplitudes of the contact point are in the Z direction. The lowest velocity in the Z direction was obtained at 25 V, and it was 1.61m/s, while the highest velocity in the Z direction was obtained at 70 V, and it was 2.54 m/s. The difference between velocity amplitudes at the lowest and highest excitation voltages is 0.93 m/s or 36.6%. It can be noticed that the ratio of velocity increment to excitation voltage is 4.13 mm/s/V.

Figure 13 also presents velocity amplitudes in the X and Y directions. The lowest velocity amplitude in the X direction was obtained at 25 V and is 1.44 m/s, while the highest velocity amplitude in the X direction was obtained at 70 V and is 2.41 m/s. The difference between the highest and lowest velocity amplitudes is 0.97 m/s or 40.23%. It was found that the ratio of velocity increment to excitation voltage is 4.31 mm/s/V. The lowest velocity amplitude in the Y direction is 1.18 m/s at 25 V, while the highest velocity amplitude is 2.21 m/s at 70 V. The difference between the lowest and highest velocity amplitudes is 1.03 m/s or 46.72%. The ratio of velocity amplitude increment to excitation voltage is 4.57 mm/s/V.

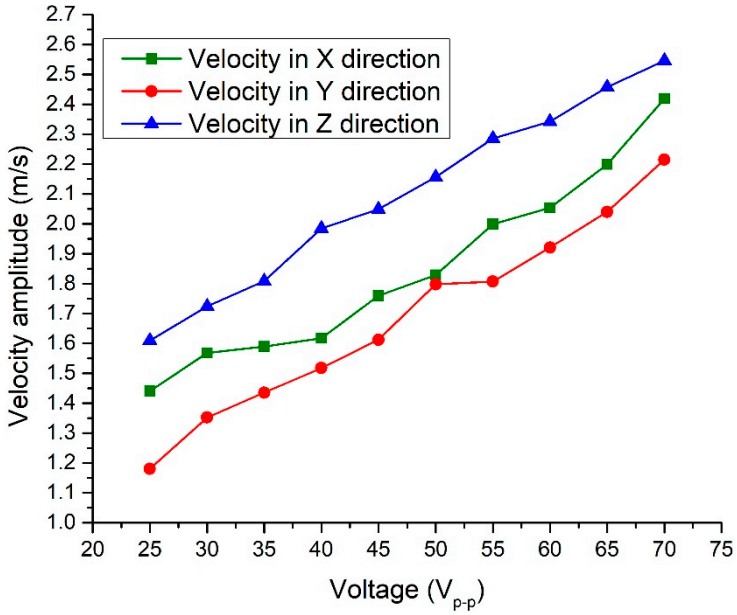

Figure 13. Velocity amplitude of the contact point in the XYZ directions versus driving voltage.

Based on the obtained results it can be concluded that the contact point velocities in the XYZ directions almost linearly depend on the excitation voltage, and differences between the velocity amplitudes in the XYZ directions are small. On the other hand, the actuator exhibits low response to excitation voltage increment due to high stiffness of the waveguide.

Dependence of the rotation speed of the rotor on excitation voltage was investigated at a constant preload force of 98.58 mN. The rotation speed was measured by employing the experimental setup (Figure 10). The results are shown in Figure 14.

As can be seen in Figure 14, rotation speed varied from 20 RPM at 100 V to 115 RPM at 350 V. The difference between the lowest and highest rotation speeds is 95 RPM or 82.6 %. The ratio between rotation speed and excitation voltage increment is 0.63 RPM/V. Figure 14 shows that the relation of rotation speed to excitation voltage is almost linear. Considering the results of the experimental investigations, it can be concluded that actuator operation is based on the superposition of the first longitudinal and second bending vibration modes. Moreover, the actuator can provide stable and well-predictable displacement and velocity of the contact point, as well as rotation speed of the rotor. On the other hand, the actuator has a relatively low response to excitation voltage amplitude increment, which is influenced by the high structural stiffness of the waveguide.

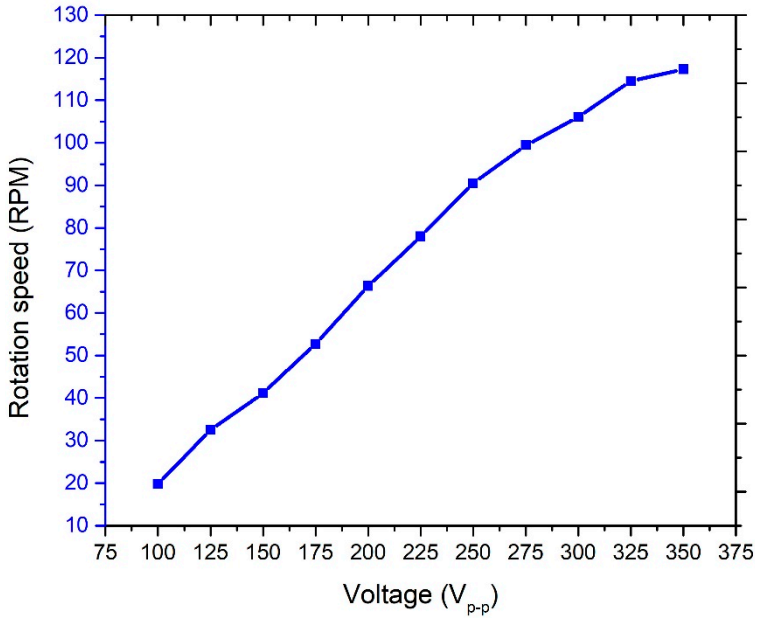

Figure 14. Rotation speed versus excitation amplitude at constant preload force.

In order to evaluate the performance of the proposed actuator, a comparison between different designs of traveling wave actuators was made. The comparison is given in Table 4.

Table 3 presents a comparison between the proposed actuator and traveling wave actuators reported previously. In order to compare the constructions, the ratio of maximum rotation speed to excitation voltage was calculated. As shown in Table 4, the actuator reported by Kanda et al. [13] generates a significantly higher ratio of rotation speed to excitation voltage compared to the proposed actuator—more than 89 times higher. On the other hand, the actuators proposed by Jin and Zhao [15] and Ting et al. [16] generate notably lower ratios compared to the proposed actuator—approximately 2 and 16, respectively.

Table 4. Comparison of different traveling wave actuators.

Authors	Operation Frequency (kHz)	Excitation Voltage (V_{p-p})	Maximum Rotation Speed (RPM)	Ratio of Maximum Rotation Speed to Excitation Voltage (RPM/V_{p-p})
Kanda et al. [13]	67	40	1000	25
Jin and Zhao [15]	48.62	300	50	0.166
Ting et al. [16]	44	200	4.16	0.0208
Proposed actuator	51.2	350	115	0.328

5. Conclusions

A new type of traveling wave actuator based on a special waveguide was developed. The operation of the actuator is based on the superposition of the first longitudinal and second bending vibration modes. The conical hole of the actuator allows the construct to amplify the displacement amplitudes of the contact point vibrations. Optimization of the conical hole and the stator dimensions allowed us to minimize the difference between the natural frequencies of the first longitudinal and second bending vibration modes to 43 Hz. The results of the numerical and experimental investigations confirmed the operating principle of the actuator and showed that the actuator can generate traveling wave vibrations. The numerically calculated maximum displacement amplitudes in the X, Y, and Z directions reached 6.24 μm, 3.1 μm, and 47.53 μm, respectively. On the other hand, experimental investigations showed displacement amplitudes from 45.4 μm to 87.5 μm in the X direction, from 60.1 μm to 92.5 μm in the Y direction, and from 61.6μm to 89.1 μm in the Z direction. Therefore, the differences between the results of the numerical and experimental investigations are notable. Mostly, such mismatches in the results are influenced by differences between the numerical model and the prototype of the actuator, i.e., clamping, characteristics of the materials, errors of manufacturing and the numerical model, and constructional drawbacks related to the thread junction between the lower and upper parts of the actuator. At high operation frequency, large displacement amplitudes in the longitudinal direction create looseness in the thread junction and prevent full velocity transfer to the top surface of the actuator during operation.

On the other hand, the rotation speed of the rotor almost linearly depends on the excitation voltage. A maximum rotation speed of the rotor of 115 RPM at 350 V was obtained.

Author Contributions: Conceptualization, D.M. (Dalius Mažeika); Data curation, A.Č.; Investigation, A.Č.; Supervision, D.M. (Dalius Mažeika); Validation, D.M. (Daiva Makutėnienė); Visualization, D.M. (Daiva Makutėnienė); Writing—original draft, A.Č. and D.M. (Daiva Makutėnienė); Writing—review and editing, D.M. (Dalius Mažeika). All authors have read and agreed to the published version of the manuscript.

Funding: This research has received funding from the European Regional Development Fund (Project No 01.2.2-LMT-K-718-01-0010) under a grant agreement with the Research Council of Lithuania.

Conflicts of Interest: The authors declare no conflict of interest.

References

1. Wang, S.; Rong, W.; Wang, L.; Xie, H.; Sun, L.; Mills, J.K. A survey of piezoelectric actuators with long working stroke in recent years: Classifications, principles, connections and distinctions. *Mech. Syst. Signal. Process.* **2019**, *123*, 591–605. [CrossRef]
2. Uchino, K.; Cagatay, S.; Koc, B.; Dong, S.; Bouchilloux, P.; Strauss, M. Micro piezoelectric ultrasonic motors. *J. Electroceramics.* **2004**, *13*, 393–401. [CrossRef]
3. Karl, S.; Koc, B. Piezoelectric motors, an overview. *Actuators* **2016**, *5*, 6.
4. Uchino, K. Piezoelectric ultrasonic motors: Overview. *Smart Mater. Struct.* **1998**, *7*, 273–285. [CrossRef]
5. Ragulskis, K.; Bansevicius, R.; Barauskas, R.; Kulvietis, G. *Vibro-Motors for Precision Micro-Robots, Application of Vibration Series*; Rivin, E., Ed.; Hemisphere Publishing Co.: Detroit, MI, USA, 1988.
6. Wu, J.; Mizuno, Y.; Nakamura, K. A traveling-wave ultrasonic motor utilizing a ring-shaped alumina/PZT vibrator. *Smart Mater. Struct.* **2019**, *28*, 125017. [CrossRef]

7. Zhou, Y.; Chang, J.; Liao, X.; Feng, Z. Ring-shaped traveling wave ultrasonic motor for high-output power density with suspension stator. *Ultrason* **2020**, *102*, 106040. [CrossRef] [PubMed]
8. Zhang, J.; Yang, L.; Chen, H.; Ma, C.; Shen, X.; Chen, L. Design of travelling-wave rotating ultrasonic motor under high overload environments: Impact dynamics simulation and experimental validation. *Appl. Sci.* **2019**, *9*, 5309. [CrossRef]
9. Zhang, J.; Yang, L.; Ma, C.; Ren, W.; Zhao, C.; Wang, F. Improving efficiency of traveling wave rotary ultrasonic motor by optimizing stator. *Rev. Sci. Instrum.* **2019**, *90*, 056104. [CrossRef] [PubMed]
10. Zheng, W.; Zhou, J.; Ruan, Y. Effects of ultrasonic motor stator teeth height on start reliability. *Energy Harvest. Syst.* **2015**, *2*, 153–156. [CrossRef]
11. Liu, J.; Niu, Z.; Zhu, H.; Zhao, C. Design and experiment of a large-aperture hollow traveling wave ultrasonic motor with low speed and high torque. *Appl. Sci.* **2019**, *9*, 3979. [CrossRef]
12. Zhao, C. Ultrasonic motors. In *Technologies and Applications*; Science Press: Beijing, China, 2010; pp. 23–27. ISBN 978-7-03-029018-9.
13. Kanda, T.; Makino, A.; Oomori, Y.; Suzumori, K. A cylindrical micro-ultrasonic motor using micro machined bulk piezoelectric vibrator with glass case. *Jpn. J. Appl. Phys.* **2006**, *45*, 4767–4769. [CrossRef]
14. Dong, Z.; Yang, M.; Chen, Z.; Xu, L.; Meng, F.; Ou, W. Design and performance analysis of a rotary traveling wave ultrasonic motor with double vibrators. *Ultrasonics* **2016**, *71*, 134–141. [CrossRef] [PubMed]
15. Jin, J.; Zhao, C. A novel traveling wave ultrasonic motor using a bar shaped transducer. *J. Wuhan Univ. Technol. Mater. Sci. Ed.* **2008**, *23*, 961–963. [CrossRef]
16. Ting, Y.; Lee, Y.; Tsai, Y.; Chen, C. Stator design of a 2DOF traveling-wave rotary piezoelectric motor. In Proceedings of the 2008 IEEE International Conference on Robotics and Biomimetics, Bangkok, Thailand, 22–25 February 2009; pp. 493–498.
17. Čeponis, A.; Mažeika, D.; Bansevičius, R.; Bakanauskas, V. Piezoelectric actuator with traveling wave waveguide. *J. Vibroengineering* **2016**, *18*, 2936–2946. [CrossRef]